On the Feasibility of Radiomic Analysis for the Detection of Breast Lesions in Speed-of-Sound Images of the Breast

Andres F. Vargas, Angie Hernández, Ana Ramirez, and Said Pertuz(✉)

Universidad Industrial de Santander, 680002 Bucaramanga, Colombia
spertuz@uis.edu.co

Abstract. Recent non-linear ultrasound imaging methods estimate acoustic tissue properties, such as speed-of-sound (SOS), density, and compressibility, among others. These methods can be used to generate 2D reconstructions of the properties of inner structures of the breast for further analysis. Due to differences in the acoustic properties between cancerous and normal tissues, these reconstructions are particularly attractive for computerized analysis. In this work, we explored the feasibility of using radiomic analysis on SOS images for breast lesion detection. We performed an in-silico analysis of SOS slices extracted from 120 3D virtual breast phantoms and built a system based on radiomic features extracted from SOS images for the detection of breast masses. We measured the performance of the system in terms of the area under the ROC curve (AUC) with 95% confidence intervals (CI). We also compared the performance of lesion detection from SOS images against a model trained with synthetic mammograms generated from the same breast phantoms. Radiomic analysis on SOS images yielded statistically significant results with AUCs of 0.73 (CI: 0.64–0.82), 0.89 (CI: 0.83–0.95), and 0.94 (CI: 0.89–0.98) at pixel-size of 1.5, 2.0 and 2.5 mm respectively. Radiomic analysis on mammograms showed lower performance with an AUC of 0.62 (CI: 0.52–0.72). Our evidence suggests that the use of SOS images, paired with radiomic analysis, could aid on the detection of breast masses that are hard to recognise using digital mammography. Further investigation on ultrasound-based reconstruction of SOS images of the breast is warranted.

Keywords: Ultrasound · Mammography · Full waveform inversion · Breast cancer · Lesion detection · Radiomic analysis

1 Introduction

As of 2021, breast cancer was the most diagnosed cancer in women in the United Kingdom and one of the leading causes of cancer-related deaths. Early cancer

This work was partially funded by MINCIENCIAS projects number 110284467139.
A. F. Vargas and A. Hernández—Equally contributing authors.

G. Yang et al. (Eds.): MIUA 2022, LNCS 13413, pp. 798–813, 2022.
https://doi.org/10.1007/978-3-031-12053-4_59

detection is crucial for better patient prognosis, and mammography is the primary screening modality used for this task. The utility of mammography screening has been reflected in a reduction on breast cancer mortality [5]. Despite its advantages, mammography has the downside of exposing the patient to ionising radiation, and has been shown to have a decreased sensitivity in radiologically dense breasts due to the overlaying of dense tissues [9]. As an alternative to mammography, ultrasound-based imaging is a non-invasive, radiation-free modality that uses high-frequency sound waves to retrieve information about the inner structures of the breast. Although breast ultrasound has a higher false positive rate, and often requires to be supplemented by mammography for screening purposes, it has shown a higher sensitivity in denser breasts and better diagnostic accuracy on younger patients than digital mammography [4,29].

Due to the advantages of ultrasound imaging, the research community has invested a lot of efforts in improving this technique as well as in developing new ultrasound-based imaging methods [23,26]. Ultrasound imaging uses high frequency sound waves to scan the interior of an organ. Reconstruction methods, such as full-waveform inversion (FWI) solve the wave equation using all the information in the recorded wavefield, including multiple scaterring, dispersion and diffraction effects [24,28]. As a result, modern ultrasound-based imaging techniques allow for a more accurate estimation of acoustic properties of the tissue. FWI has shown superior reconstruction capacities than other ultrasound techniques when tested on data representing a slice enclosing a cancerous mass [18].

For diagnosis and screening purposes, we believe that one of the main advantages of ultrasound imaging compared to mammography is the direct estimation of acoustic tissue properties that are more suitable for the detection of cancer-related anomalies. Specifically, ultrasound allows for the estimation of *speed-of-sound* (SOS) propagation in the tissue. Previous researchers have measured differences between the values of these properties in cancerous and non-cancerous tissues [13,20]. As a result, we hypothesise that ultrasound-based imaging is more suitable for fully-automated, quantitative analysis of the images. Specifically, we propose that *radiomic anaysis* of SOS images can be used to detect breast lesions. Radiomic analysis refers to computerised methods that use texture features extracted from medical images for quantitative analysis [12]. Radiomic analysis has shown encouraging performance for breast cancer diagnosis using mammography [1] and classic ultrasound images [15].

In order to test our hypothesis, we conduct an in-silico experiment to measure the performance of automatic lesion detection using SOS images of breasts by means of fully-automated, computerised radiomic features. For this purpose, we generated 3D digital breast phantoms corresponding to 60 healthy breasts and 60 breasts with lesions. Subsequently we build a lesion detection system based on radiomic features extracted from SOS images. For comparison purposes, we generated mammograms of the same breast phantoms by simulating X-ray propagation. Our results demonstrate that radiomic analysis on SOS images at pixel-size(Δ) of 1.5, 2.0 and 2.5 mm (AUCs of 0.73, 0.89, and 0.94) significantly

outperforms radiomic analysis in the mammograms (AUC of 0.62). Our findings suggest that SOS images can be used for lesion detection via radiomics analysis. This highlights the potential of ultrasound based imaging and the exploration of imaging modalities that can characterise different acoustic properties of the tissue.

2 Materials and Methods

In this section we describe how we generated a virtual breast cohort for the in-silico experiments as well as the proposed method for the detection of breast lesions from SOS images. Specifically, the generation of 3D breast phantoms and SOS images are described in Sects. 2.1 and 2.2, respectively. Because we compare our approach with radiomic analysis in mammography images, we also describe the generation of synthetic mammograms in Sect. 2.3. Finally, in Sect. 2.4, we describe the extraction of radiomic features and the construction of the lesion detection model.

2.1 Virtual Breast Cohort

The generation of digital breast phantoms is an open problem in the community and several modelling systems have been developed to date [3,17,30]. The aim is to generate realistic and anatomically accurate models often utilised for the development and validation of new imaging techniques [10]. For our experiments, we used the simulation software developed for the Virtual Imaging Clinical Trial for Regulatory Evaluation (VICTRE). The VICTRE project was carried out by the U.S. Food and Drug Administration in order to reproduce virtual clinical trials, which are often expensive in time and resources [2,25]. We selected this simulator due to its adoption in the evaluation of X-ray breast imaging systems [10,19]. The VICTRE simulator generates voxelised breast phantoms with a pixel-size of 50 µm that contain the different tissues of the breast [7], with the possibility of inserting spiculated masses and calcifications. The phantoms are customisable in total volume, fat percentage, distance from the chest wall to the nipple, and other physiological characteristics. Figure 1 shows an example of a breast phantom and corresponding 2D slices. The different tissue types in the breast phantom and their properties are described in Sect. 2.2.

For our experiments, we generated a virtual cohort consisting of 120 subjects: 60 phantoms without a spiculated mass (controls) and 60 phantoms with a spiculated mass (cases) with a volume of 77.7 mm^3 and diameter of 5 mm. The only difference between cases and controls phantoms is the insertion of the spiculated mass in the cases. In order to conduct experiments in a realistic cohort, we simulated four types of breast phantoms, each reflecting different glandularity types. As reference, we used the distribution of glandularity types found in case-control studies of screening mammography (see [21]). Table 1 summarizes the main features of our virtual cohort.

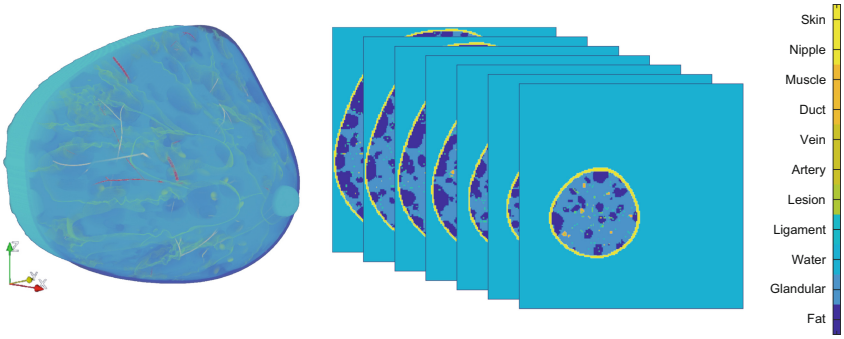

Fig. 1. (a) Visualisation of a virtual 3D breast phantom. (b) Slices taken at different positions along the X axis. Each colour identifies a different type of tissue in the slices.

Table 1. Summary of the virtual cohort.

Glandularity type	Mean percent density (%)	Mean volume (cm^3)	No. phantoms (%)
Dense	50	141.8	4
Heterogeneously dense	41	255.7	48
Scattered fibroglandular	25	497.7	56
Fatty	17	749.1	12

2.2 Speed-of-Sound Images

In order to assess the feasibility of using SOS images for lesion detection, we generate a stack of bidimensional SOS slices from each 3D breast phantom. Previous works have investigated and measured SOS values in both normal and cancerous breast tissue [6,14]. Therefore, we extract 2D SOS images by replacing each tissue type in the phantoms by their corresponding SOS values as reported in the literature. In Table 2, we summarise the SOS values used for each type of tissue. This approach assumes an ideal reconstruction process of the SOS images. In practice, the quality of the SOS slices obtained via ultrasound imaging will depend on several variables, such as the imaging architecture and the reconstruction techniques. The investigation of imaging architectures and reconstruction techniques for ultrasound-based imaging of the breast is beyond the scope of this work and the utilisation of ideally-reconstructed SOS images is sufficient for our feasibility study.

Table 2. Speed-of-sound (SOS) propagation values for each type of tissue. Tissues are ordered in increasing value of SOS.

Tissue	Speed-of-sound propagation [m/s]	Reference
Fat	1440.0	Hasgal *et al.*., 2012 [8]
Glandular	1505.0	Hasgal *et al.*., 2012 [8]
Water	1520.0	Ramirez *et al.*., 2017 [22]
Ligament	1525.0	Foster *et al.*, 1984 [6]
Lesion	1572.0	Foster *et al.*, 1984 [6]
Artery	1578.2	Hasgal *et al.*., 2012 [8]
Vein	1578.2	Hasgal *et al.*., 2012 [8]
Duct	1588.0	Klock *et al.*., 2016 [11]
Muscle	1588.4	Hasgal *et al.*., 2012 [8]
Nipple	1624.0	Hasgal *et al.*., 2012 [8]
Skin	1624.0	Hasgal *et al.*., 2012 [8]

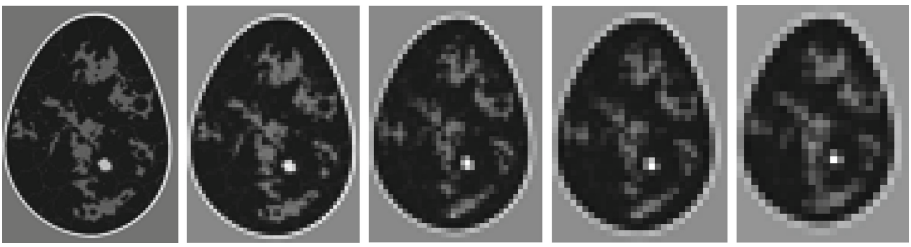

Fig. 2. SOS images for different pixel-sizes. From left to right: 1.0, 1.5, 2.0, 2.5 and 3.0 mm.

Previous work has demonstrated the generation of ultrasound-based reconstructions with pixel-size (Δ) down to 0.5 mm [16]. These pixel-sizes are an order of magnitude lower than in mammography, in which pixel-size of 0.05 mm are readily attainable by modern mammographic systems. In order to assess the impact of the pixel-size on the performance of the system, we generate SOS images at pixel-sizes between 1.0 mm and 3.0 mm (see Fig. 2).

2.3 Digital Mammography Simulation

Being the most widely used breast screening modality, we used radiomic analysis of mammograms for comparison. For this purpose, we generated digital mammograms from each of the virtual phantoms of the study cohort. Specifically, we used the open-source X-ray imaging simulation code MC-GPU [2], in order to simulate the image acquisition process of an actual mammography acquisition device, namely, a Siemens Mammomat Inspiration. MC-GPU is a GPU-accelerated Monte Carlo simulation of X-ray interaction with matter; the code models the source, primary radiation beam, scattering and absorption events,

and direct-conversion detector, among other aspects that influence mammography acquisition. For each phantom, we simulated the physical compression of the breast in the craniocaudal direction using VICTRE, and obtained one craniocaudal mammography image, thus rendering a dataset of 120 mammograms, 60 cases, and 60 controls. Due to differences in breast volume, the image size of the mammograms were 1000×2010 pixels for dense and heterogeneous phantoms, and 1500×2010 pixels for scattered and fatty phantoms. The pixel size in every case was $85\,\mu$m.

2.4 Lesion Detection

We built a system for the detection of lesions in SOS images in two phases. In the training phase, we train a *slice classifier* that takes one SOS slice as input and generates a score with the likelihood of a lesion. In the second phase, the testing phase, the slice classifier is used to generate a score in each SOS slice of a test phantom, and a *greedy* classifier estimates the score at the breast level. We refer to this second phase as the *breast classifier*. To construction of the slice classifier and the breast classifier are detailed below.

Slice classifier: as shown in Fig. 3, the slice classifier is trained with SOS images extracted from the controls and the cases, with each phantom of the training set contributing with one SOS image. Because the lesions only occupy a very small volume of the 3D breast phantoms, SOS images in the cases are selected so that the lesion is visible. In the controls, the SOS images are selected on the same position as in the corresponding case. This allows to generate a training set of 2D SOS images with and without lesions. Figure 4 shows a pair of SOS images with and without lesions.

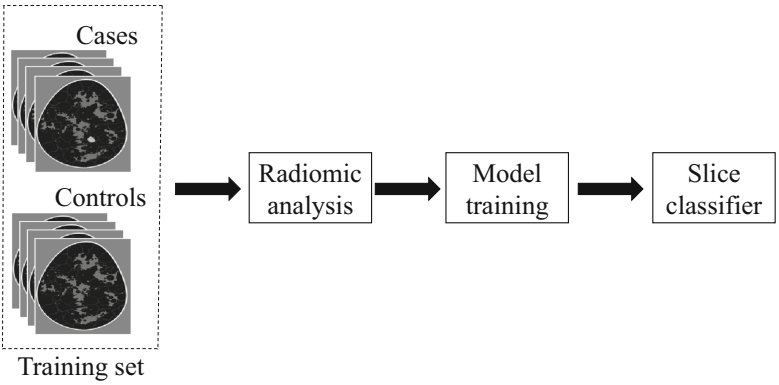

Fig. 3. Training of the slice classifier.

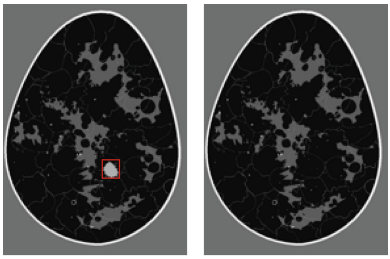

(a) (b)

Fig. 4. Example of SOS images used to train the slice classifier. (a) SOS image from a case retrieved at a position where the lesion is visible. The lesion is highlighted by the red square. (b) SOS image from the control corresponding to the same case and position of (a). (Color figure online)

Back to the slice classifier in Fig. 3, each image in this training set goes through a *radiomic analysis* block in order to extract texture descriptors. The aim or radiomic analysis is to generate quantitative measures that describe the textural appearance of the image. In turn, these measures are used to build insightful models with supervised machine learning algorithms; in the case at hand, the model corresponds to a classification model to differentiate SOS images with and without lesions.

By their working principles, radiomic features can be categorised in five groups: statistical features, which describe the histogram of gray level values of the image; gray-level co-occurrence features that describe the statistical spatial distribution of co-occurrent pixel intensities; gray-level run-length features that describe the consecutive intensity values of the image (run-lengths); structural features that describe the topological and geometric elements that constitute the image; and finally, spectral features, which are features calculated from the frequency-spatial domain of the image. In this work, we extract 33 radiomic features from the breast region in our dataset using OpenBreast [21]. OpenBreast is an open source tool for radiomic analysis.

Finally, the *model training* block in Fig. 3 uses extracted radiomic features to build the slice classifier by means of logistic regression with sequential forward feature selection [27].

Breast classifier: from the training phase, the slice classifier should be able to classify SOS images with and without lesions. However, at testing time, each breast phantom is comprised of a full stack of 2D SOS images, whereas the potential location of the lesions is unknown. For this reason, the aim of the breast classifier is to analyse the full stack of SOS images of a phantom in order to generate a single estimate at the breast level.

Because SOS images are generated by slicing the 3D breast volume, not all SOS images in the stack have useful information. As shown in Fig. 5, the trailing 2D slices of a phantom correspond to the nipple region, whereas the leading slices

correspond to the pectoralis muscle. For this reason, the slices at the trailing 10% and leading 30% of the breast volume are discarded, and only the SOS images of the remaining breast volume are processed.

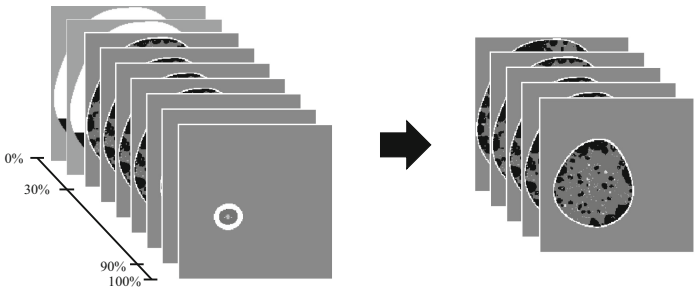

Fig. 5. Selection of slices between 30% and 90% for the subsequent analysis by the breast classifier.

Once the relevant slices have been selected by the procedure described above, the *slice classifier* that was trained in the previous stage is used to generate a classification score for each 2D slice in the breast. This generates an ordered sequence of scores, Score 1 to Score n in Fig. 6. In order to attenuate noise in the score estimate in individual slices, the *greedy classifier* of Fig. 6 works by computing a 3-tap moving average on the sequence of scores and retrieves the maximum score value of the sequence. This is a very simple method that yields a high score as long as the slice classifier detects at least one slice with a lesion in the full stack of slices of the breast.

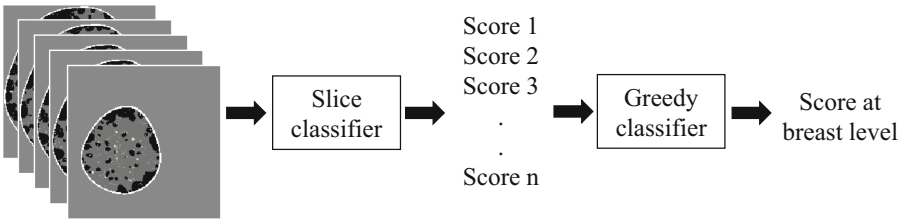

Fig. 6. Breast classifier. The input is a stack of n SOS images and the output is a single score for the breast.

Table 3. AUC of the slice classifier using different pixel-sizes of SOS images.

Pixel-size (Δ) [mm]	AUC (95% Confidence interval)
1.0	0.81 (0.74–0.89)
1.5	0.88 (0.81–0.94)
2.0	0.97 (0.94–1.00)
2.5	0.95 (0.90–0.99)
3.0	0.96 (0.93–1.00)

3 Experiments and Results

For all experiments, the results reported correspond to a randomised 5-fold cross validation. In each fold, the slice classifier is built using SOS images retrieved only from the training set and the breast classifier generates a score for each virtual breast in the test set. Performance was measured in terms of the area under the receiver operating characteristic (ROC) curve (AUC). The ROC curve is a graphical plot that illustrates the diagnostic ability of a binary classifier system.

3.1 Performance at the Slice Level

Because the breast classifier fully relies on the performance of the slice classifier, in this section we first report the performance in the classification of SOS images. At the image level, the greedy classifier is not used nor needed. Experiments are performed under the same conditions for each pixel-size of SOS images, namely 1.0, 1.5, 2.0, 2.5, and 3.0 mm. Results at slice level are presented in Table 3. As highlighted in that table, SOS images at 2.0 mm pixel-size yield the best performance at the image level.

3.2 Performance at the Breast Level

In this section, we report the results on lesion detection at the breast level. For comparison purposes, we also performed radiomic analysis of synthetic mammographic images generated as described in Sect. 2.3. For this purpose, in each mammogram, we process a region of 17×17 mm^2 enclosing the location of each lesion (i.e. see Fig. 7a) for the extraction of radiomic features and the construction of a *lesion classifier*, as shown in Fig. 7b. Performance results at the breast level are presented in Table 4. In this case, SOS images outperform mammography at all pixel-sizes, with the 2.5 mm pixel-size having the best performance. Figure 8 shows the ROC curve for the three top performing pixel-sizes using SOS images and the ROC curve of the model trained using mammography.

4 Discussion

The results show that the use of SOS images outperforms synthetic mammograms to detect breast lesions in pixel-sizes between 1.0 and 2.5 mm. The pixel-size that performs the highest at the breast level is 2.5 mm. Figure 9a shows

Table 4. AUC for the breast classifier using different pixel-sizes of SOS images and compared whit the mammography.

Modality	Pixel-size (Δ) [mm]	AUC (95% Confidence interval)
SOS image	1.000	0.67 (0.57–0.77)
	1.500	0.73 (0.64–0.82)
	2.000	0.89 (0.83–0.95)
	2.500	0.94 (0.89–0.98)
	3.000	0.59 (0.49–0.69)
Mammography	0.085	0.62 (0.52–0.72)

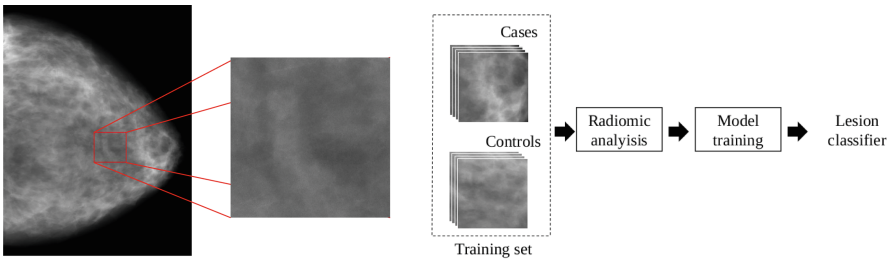

Fig. 7. Construction of lesion classifier for mammograms. (a) The region of interest corresponds to an area of 17 $\times$ 17 mm^2 surrounding the location of the spiculated mass. (b) Training of the classifier.

the distribution of case and control scores using the breast classifier at 2.5 mm pixel-size, and Fig. 9b shows the distribution of scores using the lesion classifier on digital mammograms. This figure shows that the scores estimated using SOS images allow for a more clear discrimination between cases and controls than mammograms. The lower performance obtained using mammography images can be explained by the overlapping of the different breast tissues: since mammography can be roughly described as a projection of the breast internal structures, overlapping can have a masking effect on small elements with similar radiation density to the surrounding tissues.

Figure 10 shows the output scores, after the 3-tap moving average, for each slice of the stack of images corresponding to a case and its respective control. In said figure, scores are very similar for most case and control slices. However, for the slices close to the centre of the lesion (vertical green line), there are notable differences. This behaviour clearly discriminates cases from controls.

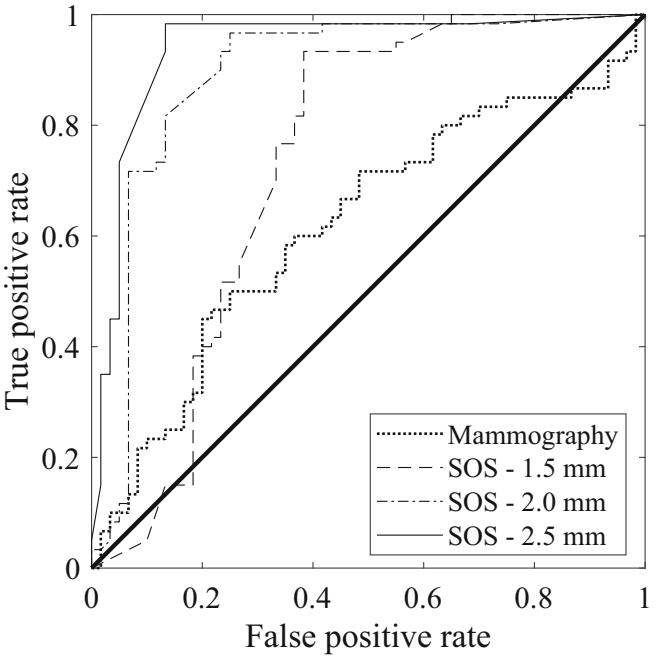

Fig. 8. ROC curves for the best-performing SOS images at breast level and mammography.

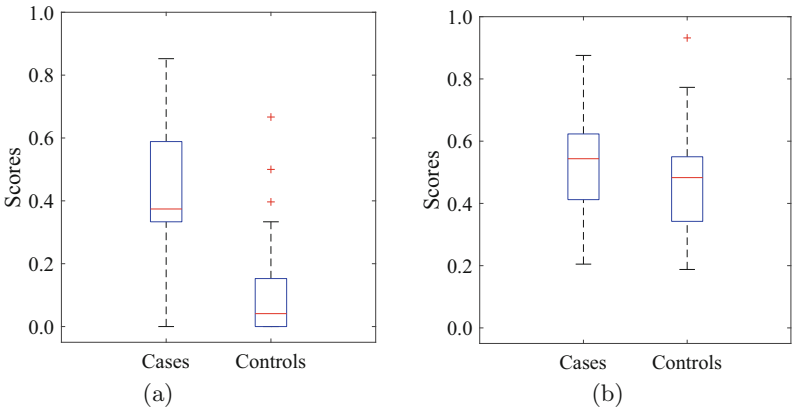

Fig. 9. Distribution of scores in cases and controls for: (a) the breast classifier using SOS images at pixel-size of 2.5 mm, and (b) the lesion classifier using mammograms.

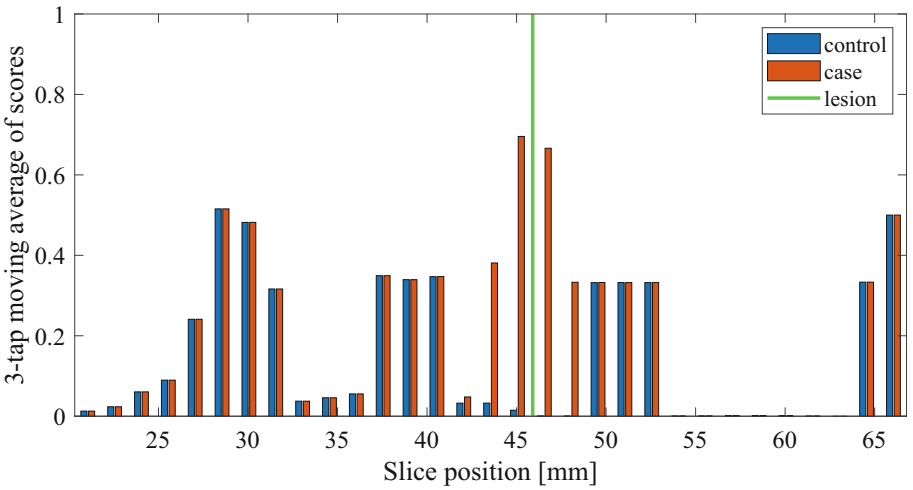

Fig. 10. Scores of the slice classifier for each slice of the stack of images corresponding to a case and its respective control. The green line represents the position of the lesion center. (Color figure online)

The sequential forward feature selection technique finds the most relevant features that the logistic regressor uses for the classification. Overall, when training the slice classifier using SOS images, the most relevant features were: statistical, gray-level co-occurrence, and gray level path length features, while for the lesion classifier using digital mammograms, the most relevant features were: structural and spectral features (see Table 5).

In this work we used SOS images that would be an ideal reconstruction of the speed of sound parameters for the breast tissues. In a real life scenario, different imaging architectures and reconstruction algorithms could affect the quality and noise level of the reconstructed images. In addition, we considered one type of lesion, spiculated masses with a volume of 77.7 mm^3; these lesions are among the most common malignant breast lesions. Future work should take into consideration the impact of the image quality on performance, as well as explore the impact of lesion size variability and consider the detection of other elements of interest, such as microcalcifications, which are typically more problematic in ultrasound imaging.

Table 5. Features selected by the model after the forward sequential feature selection, for each pixel-size of SOS images and mammography.

Feature group	Feature	SOS images					Mammography
		1.000 mm	1.500 mm	2.000 mm	2.500 mm	3.000 mm	0.085 mm
Statistical features	Minimum gray-level value				x		
	Maximum gray-level value	x	x	x	x		
	Mean gray-level value	x					
	Gray-level range	x			x	x	x
	Gray-level variance	x					
	Entropy						
	Skewness	x	x				
	Kurtosis	x	x	x	x		
	5^{th} percentile		x				
	30^{th} percentile					x	
	70^{th} percentile	x					
	90^{th} percentile						
	Balance 1	x	x				
	Balance 2	x	x				
Co-ocurrence features	Energy						
	Correlation	x	x				
	Contrast			x		x	
	Homogeneity					x	
	Entropy	x	x	x			
Run-length features	Run-length non-uniformity	x	x	x			
	Gray-level non-uniformity	x					
	Long run emphasis						
	Short run emphasis						
	Run percentage						
	High gray-level run		x				
	Low gray-level run		x				
Structural features	Gradient energy		x				
	Gradient variance	x					x
	Modified laplacian						
Spectral features	Wavelet sum						x
	Wavelet variance						
	Wavelet ratio						
	Fractal dimension						

5 Conclusions

In this work, we studied the feasibility of utilising speed-of-sound (SOS) propagation images of the breast for the detection of breast lesions via radiomic analysis. We performed an in-silico test, obtaining SOS images from a cohort of 120 3D synthetic phantoms, that were subsequently analysed at the breast level to detect breast lesions. We compared the performance of using SOS images against using the most common imaging modality for breast cancer diagnosis and detection, namely mammography. The results show that the performance using SOS images at the breast level outperforms mammography at pixel-sizes

between 1.0 and 2.5 mm. This indicates that using these novel ultrasound-based imaging modalities as an adjunct for breast lesion detection would be feasible. It also shows the importance of exploring imaging modalities that can resolve tissue descriptors that are not classically used, such as speed SOS.

Novel methods for ultrasound-based medical imaging have recently been developed. These novel methods have the ability to construct a profile of some physical properties of the organ, such as SOS. More common imaging modalities for breast cancer screening, such as mammography or breast tomosynthesis, have the downside of being essentially projections of the breast; their capacity to resolve areas of interest depends on the attenuation contrast between breast elements, but the superposition of tissues, and the similar radio-density of interesting elements such as cancerous masses and fibroglandular tissue, can obscure these areas and result in missed cases. The use of novel technologies that allow for the characterisation of other properties of the breast, and other types of 2D visualisations such as SOS profiles at specific positions in the organ, could be explored to overcome the obstacles encountered with currently widespread modalities.

References

1. Al-Antari, M.A., Han, S.M., Kim, T.S.: Evaluation of deep learning detection and classification towards computer-aided diagnosis of breast lesions in digital x-ray mammograms. Comput. Methods Progr. Biomed. **196**, 105584 (2020)
2. Badal, A., Sharma, D., Graff, C.G., Zeng, R., Badano, A.: Mammography and breast tomosynthesis simulator for virtual clinical trials. Comput. Phys. Commun. **261**, 107779 (2021)
3. Barufaldi, B., et al.: Computational breast anatomy simulation using multi-scale Perlin noise. IEEE Trans. Med. Imaging **40**(12), 3436–3445 (2021)
4. Devolli-Disha, E., Manxhuka-Kërliu, S., Ymeri, H., Kutllovci, A.: Comparative accuracy of mammography and ultrasound in women with breast symptoms according to age and breast density. Bosn. J. Basic Med. Sci. **9**(2), 131 (2009)
5. Dibden, A., Offman, J., Duffy, S.W., Gabe, R.: Worldwide review and meta-analysis of cohort studies measuring the effect of mammography screening programmes on incidence-based breast cancer mortality. Cancers **12**(4), 976 (2020)
6. Foster, F., Strban, M., Austin, G.: The ultrasound macroscope: initial studies of breast tissue. Ultrason. Imaging **6**(3), 243–261 (1984)
7. Graff, C.G.: A new, open-source, multi-modality digital breast phantom. In: Medical Imaging 2016: Physics of Medical Imaging, vol. 9783, p. 978309. International Society for Optics and Photonics (2016)
8. Hassgal, P.A., et al.: IT'IS database for thermal and electromagnetic parameters of biological tissues version 4.1 (2022)
9. Ho, W., Lam, P.: Clinical performance of computer-assisted detection (CAD) system in detecting carcinoma in breasts of different densities. Clin. Radiol. **58**(2), 133–136 (2003)
10. Kiarashi, N., et al.: Development and application of a suite of 4-D virtual breast phantoms for optimization and evaluation of breast imaging systems. IEEE Trans. Med. Imaging **33**(7), 1401–1409 (2014)

11. Klock, J.C., Iuanow, E., Malik, B., Obuchowski, N.A., Wiskin, J., Lenox, M.: Anatomy-correlated breast imaging and visual grading analysis using quantitative transmission ultrasound^{TM}. Int. J. Biomed. Imaging **2016**, 7570406 (2016)
12. Lambin, P., et al.: Radiomics: the bridge between medical imaging and personalized medicine. Nat. Rev. Clin. Oncol. **14**(12), 749–762 (2017)
13. Li, C., Duric, N., Huang, L.: Clinical breast imaging using sound-speed reconstructions of ultrasound tomography data. In: Medical Imaging 2008: Ultrasonic Imaging and Signal Processing, vol. 6920, pp. 78–86. SPIE (2008)
14. Li, C., Duric, N., Littrup, P., Huang, L.: In vivo breast sound-speed imaging with ultrasound tomography. Ultrasound Med. Biol. **35**(10), 1615–1628 (2009)
15. Liu, B., Cheng, H.D., Huang, J., Tian, J., Tang, X., Liu, J.: Fully automatic and segmentation-robust classification of breast tumors based on local texture analysis of ultrasound images. Pattern Recognit. **43**(1), 280–298 (2010)
16. Lucka, F., Pérez-Liva, M., Treeby, B.E., Cox, B.T.: High resolution 3D ultrasonic breast imaging by time-domain full waveform inversion. Inverse Prob. **38**(2), 025008 (2021)
17. Omer, M., Fear, E.: Anthropomorphic breast model repository for research and development of microwave breast imaging technologies. Sci. Data **5**(1), 1–10 (2018)
18. Ozmen, N., Dapp, R., Zapf, M., Gemmeke, H., Ruiter, N.V., van Dongen, K.W.: Comparing different ultrasound imaging methods for breast cancer detection. IEEE Trans. Ultrason. Ferroelectr. Freq. Control **62**(4), 637–646 (2015)
19. Park, S., Villa, U., Su, R., Oraevsky, A., Brooks, F.J., Anastasio, M.A.: Realistic three-dimensional optoacoustic tomography imaging trials using the VICTRE breast phantom of FDA. In: Proceedings of the SPIE 11240, Photons Plus Ultrasound: Imaging and Sensing, vol. 11240, p. 112401H, March 2020
20. Pei, Y., Zhang, G., Zhang, Y., Zhang, W.: Breast acoustic parameter reconstruction method based on capacitive micromachined ultrasonic transducer array. Micromachines **12**(8), 963 (2021)
21. Pertuz, S., et al.: Clinical evaluation of a fully-automated parenchymal analysis software for breast cancer risk assessment: a pilot study in a Finnish sample. Eur. J. Radiol. **121**, 108710 (2019)
22. Ramirez, A.B., Abreo, S.A., van Dongen, K.W.: Selecting the number and location of sources and receivers for non-linear time-domain inversion. In: 2017 IEEE International Ultrasonics Symposium (IUS), pp. 1–3 (2017)
23. Ruiter, N., Zapf, M., Dapp, R., Hopp, T., Kaiser, W., Gemmeke, H.: First results of a clinical study with 3D ultrasound computer tomography. In: 2013 IEEE International Ultrasonics Symposium (IUS), pp. 651–654 (2013)
24. Sandhu, G., Li, C., Roy, O., Schmidt, S., Duric, N.: Frequency domain ultrasound waveform tomography: breast imaging using a ring transducer. Phys. Med. Biol. **60**(14), 5381 (2015)
25. Sharma, D., et al.: Technical note: in silico imaging tools from the VICTRE clinical trial. Med. Phys. **46**(9), 3924–3928 (2019). cited by: 16
26. Taskin, U., van der Neut, J., van Dongen, K.W.: Redatuming for breast ultrasound. In: 2018 IEEE International Ultrasonics Symposium (IUS), pp. 1–9 (2018)
27. Ververidis, D., Kotropoulos, C.: Sequential forward feature selection with low computational cost. In: 2005 13th European Signal Processing Conference, pp. 1–4. IEEE (2005)
28. Virieux, J., Operto, S.: An overview of full-waveform inversion in exploration geophysics. Geophysics **74**(6), WCC1–WCC26 (2009)

29. Ying, X., Lin, Y., Xia, X., Hu, B., Zhu, Z., He, P.: A comparison of mammography and ultrasound in women with breast disease: a receiver operating characteristic analysis. Breast J. **18**(2), 130–138 (2012)
30. Zastrow, E., Davis, S.K., Lazebnik, M., Kelcz, F., Veen, B.D., Hagness, S.C.: Development of anatomically realistic numerical breast phantoms with accurate dielectric properties for modeling microwave interactions with the human breast. IEEE Trans. Biomed. Eng. **55**(12), 2792–2800 (2008)